ADVANCED OPTICAL MATERIALS
www.advopticalmat.de

$MgSiP_2$: An Infrared Nonlinear Optical Crystal with a Large Non-Resonant Phase-Matchable Second Harmonic Coefficient and High Laser Damage Threshold

Jingyang He, Yingdong Guan, Victor Trinquet, Guillaume Brunin, Ke Wang, Robert Robinson, Rui Zu, Suguru Yoshida, Seng Huat Lee, Yu Wang, Yanglin Zhu, Gian-Marco Rignanese, Zhiqiang Mao,* and Venkatraman Gopalan**

Superior infrared nonlinear optical (NLO) crystals are in urgent demand in the development of lasers and optical technologies for communications and computing. The critical challenge is to find a crystal with large non-resonant phase-matchable NLO coefficients and high laser damage threshold (LDTs) simultaneously, which however scale inversely. This work reports such a material, $MgSiP_2$, that exhibits a large second harmonic generation (SHG) coefficient of $d_{14} \approx d_{36} = 89 \pm 5$ pm V^{-1} at 1550 nm fundamental wavelength, surpassing the commercial NLO crystals $AgGaS_2$, $AgGaSe_2$, and $ZnGeP_2$. First principles theory reveals the polarizability and geometric arrangement of the [SiP_4] tetrahedral units as the origin of this large nonlinear response. Remarkably, it also exhibits a high LDT value of 684 GW cm^{-2}, which is six times larger than $ZnGeP_2$ and three times larger than $CdSiP_2$. It has a wide transparency window of 0.53–10.35 µm, allowing broadband tunability. Further, it is Type I and Type II phase-matchable with large effective SHG coefficients of $d_{eff,I} \approx 80.2$ pm V^{-1} and $d_{eff,II} \approx 73.4$ pm V^{-1}. The outstanding properties of $MgSiP_2$ make it a highly attractive candidate for optical frequency conversion in the infrared.

1. Introduction

In recent years, there has been a surge in searching for high-performance nonlinear optical (NLO) crystals in the infrared region.[1–6] Because of a dearth of all-solid-state high-power infrared lasers, frequency conversion through combining or splitting photons, such as sum (SFG) and difference (DFG) frequency generation using NLO crystals, is still the primary approach to generating infrared light. Many oxide crystals are widely used, such as β-BaB_2O_4 (BBO),[7] $LiNbO_3$,[8] and LiB_3O_5 (LBO);[9] however, they are not suitable for infrared applications due to their strong multiphoton absorption. The current benchmark infrared NLO crystals are $AgGaS_2$,[10] $AgGaSe_2$ and $ZnGeP_2$.[11] These crystals with crystal formula ABC_2 all have the chalcopyrite structure derived from the zinc blende structure, except that the unit cell is twice larger than the zinc blende structure. They consist of

J. He, R. Zu, V. Gopalan
Department of Materials Science and Engineering
Pennsylvania State University
University Park, Pennsylvania 16802, USA
E-mail: jwh5890@psu.edu; vgopalan@psu.edu

Y. Guan, R. Robinson, S. Yoshida, S. H. Lee, Y. Wang, Y. Zhu, Z. Mao, V. Gopalan
Department of Physics
Pennsylvania State University
University Park, Pennsylvania 16802, USA
E-mail: zim1@psu.edu

V. Trinquet, G. Brunin, G.-M. Rignanese
Institute of Condensed Matter and Nanosciences
UCLouvain
Louvain-la-Neuve, Wallonia 1348, Belgium

K. Wang, V. Gopalan
Materials Research Institute
The Pennsylvania State University
University Park, Pennsylvania 16802, USA

S. Yoshida, S. H. Lee, Y. Wang, Y. Zhu, Z. Mao
2D Crystal Consortium
Materials Research Institute
Pennsylvania State University
University Park, Pennsylvania 16802, USA

G.-M. Rignanese
School of Materials Science and Engineering
Northwestern Polytechnical University
No. 127 Youyi West Road, Xi'an, Shaanxi 710072, P. R. China

The ORCID identification number(s) for the author(s) of this article can be found under https://doi.org/10.1002/adom.202301060

DOI: 10.1002/adom.202301060

tetrahedral building blocks AC_2 and BC_2 oriented in the same direction. The NLO responses of these microscopic units add up to give rise to a large macroscopic NLO susceptibility.[1]

Unfortunately, these commercial infrared NLO crystals all present some drawbacks limiting their further applications. For example, $AgGaS_2$ and $AgGaSe_2$ have relatively small laser damage thresholds (LDT) due to the photodarkening effect,[12–14] whereas, $ZnGeP_2$ has strong photon absorption in 1–2 μm, restraining the options of pump lasers.[15] To qualify as a good NLO crystal, it should satisfy several competing criteria, such as large SHG coefficients, high LDT values, broad transparency, and phase-matchability. However, materials with larger bandgaps generally exhibit larger LDT but smaller SHG coefficients. Chalcogenides (group VI anions: S, Se, and Te) and pnictides (group V anions: P, As, and Sb) are crystal systems long believed to be suitable for infrared NLO applications. Compared to chalcogenides, pnictides generally have more polarizable electron clouds due to the higher covalency, which is beneficial for having larger NLO susceptibility. For example, $AgGaSe_2$ and $ZnGeP_2$ both have the chalcopyrite structure, yet $ZnGeP_2$ has a higher nonlinear coefficient and larger bandgap.[16] Several pnictides (crystal formula: ABC_2) with the chalcopyrite structure such as $CdSiP_2$,[17] $CdGeAs_2$,[18] and $MgSiAs_2$[19] have been explored as infrared NLO crystals to complement the commercial ones. These crystals also consist of distorted tetrahedra (AC_4 and BC_4), which are corner-shared by the pnictide atoms and oriented in one direction, collectively leading to a large macroscopic SHG response. Among these crystals, $CdSiP_2$ has good overall properties and is the crystal to surpass in discovering new infrared NLO crystals.

Recently, another pnictide in this crystal system, $MgSiP_2$, has attracted attention as a potential infrared NLO crystal.[20–22] Chen et al. have investigated its SHG performance in the polycrystalline powder form and reported excellent powder SHG performance;[23] however, the all-important anisotropic optical properties of single crystals necessary for phase matching for high-efficiency optical frequency conversion have not been studied due to a lack of high-quality single crystals. Here, we report the synthesis of high-quality single crystals using a modified flux method as well as the complete experimental and theoretical investigation of the linear and non-resonant nonlinear optical susceptibilities to evaluate the potential of $MgSiP_2$ as a next-generation NLO material. We found that $MgSiP_2$ demonstrates a large SHG coefficient of $d_{36} = 89$ pm V^{-1} at 1550 nm fundamental wavelength, approximately three times larger than $AgGaSe_2$ and comparable to $CdSiP_2$.[17,24] It also has infrared transparency up to ≈10.35 μm, slightly larger than $CdSiP_2$ (9.5 μm),[25] allowing broadband tunability into the mid-infrared. In addition, the crystal is determined to be both Type I and Type II phase-matchable, with effective SHG coefficients of $d_{\mathrm{eff,I}}$ ≈80.2 pm V^{-1} and $d_{\mathrm{eff,II}}$ ≈73.4 pm V^{-1} at 3.5 μm fundamental wave; it is a significant advantage that $d_{\mathrm{eff,I}} \approx d_{36}$ under phase-matching conditions. In contrast, $ZnGeP_2$ and $CdSiP_2$ can only be Type I phase-matched at 3.5 μm with a $d_{\mathrm{eff,I}}$ of ≈54 and ≈60 pm V^{-1}, respectively. Importantly, $MgSiP_2$ demonstrates a giant LDT value of 684 GW cm^{-2} (measured with a femtosecond laser system: 1550 nm, 1 kHz, 100fs), six times larger than $ZnGeP_2$ and over three times larger than $CdSiP_2$. These outstanding properties make $MgSiP_2$ an outstanding NLO crystal candidate in the infrared.

2. Results and Discussion

$MgSiP_2$ single crystals are grown through the flux growth method with Sb or Sn flux modified based on previously reported methods.[26,27] Details of synthesis can be found in the Experimental Section, and the comparison of the current and previously reported methods is described in Supporting Information. It crystallizes in the space group $I\bar{4}2d$ (point group $\bar{4}2m$) and adopts a 3D chalcopyrite structure, as shown in **Figure 1**a. Similar to other chalcopyrite structured crystals, it comprises aligned MgP_4 and SiP_4 units (Figure S1, Supporting Information), allowing the superposition of the microscopic SHG response generated from these tetrahedra, which results in overall strong SHG performance. As shown in Figure S2, Supporting Information, the as-grown crystals are needle-like with typical dimensions of 0.3–0.5 mm (width) × 0.3–0.4 mm (thickness) × 2–6 mm (length). It grows along the [111] direction with two natural facets which correspond to the (112) and (101) planes. Typically, the (112) plane is larger than the (101) plane. X-ray diffraction (XRD) was performed on these two facets to confirm the chalcopyrite structure and high crystallinity, as shown in Figure 1b. The crystals are air-sensitive but stable in water. When left in the ambient atmosphere for 2 days, the surface of the crystal starts to degrade, as shown in Figure S3, Supporting Information; hence for eventual applications, the crystal surfaces will need to be sealed against air exposure. Similar procedure has also been done on other commercial crystals such as BBO.[28] Figure 1c shows the atomic resolution high-angle annular dark-field (HAADF)-STEM image taken along the [110] axis. The STEM image also illustrates that the as-grown $MgSiP_2$ crystal possesses the same structure as the previously reported one.[26]

$MgSiP_2$ was also investigated using first-principles calculations. The 8*d* Wyckoff sites (the locations of the atoms in the unit cell) for space group $I\bar{4}2d$ is (x, 0.25, 0.125). In the case of $MgSiP_2$, this internal parameter x (8*d* Wyckoff sites) in its conventional tetragonal cell is associated with the position of P atoms. The crystal structure was first fully relaxed, adopting the local-density approximation (LDA) for the exchange-correlation energy. The calculated ($a = 5.678$ Å, $c = 10.095$ Å, $x = 0.208$) and experimental ($a = 5.721$ Å, $c = 10.037$ Å, $x = 0.207$) cell and internal parameters were found to be in excellent agreement with a difference below 1%. Finally, a relaxation of the internal parameter was also performed while keeping the cell parameters a and c fixed to their experimental values. This led to $x = 0.207$ and a distortion parameter[29] $u = \frac{1}{4} + \frac{d_{Mg-P}^2 - d_{Si-P}^2}{a^2} = 0.293$ in accordance with previous investigations.[20,30] The resulting structure was used in all subsequent computations unless stated otherwise.

The band structure, shown in Figure 1d, was computed in the same framework. The predicted 1.17 eV bandgap is direct and greatly underestimates the experimental value of 2.34 eV. Such a discrepancy is inherent to DFT when using local or semi-local functionals for the exchange-correlation energy. Since optical properties are directly related to the bandgap, the latter was systematically corrected to match the experimental gap by applying a scissor shift to all conduction bands. The band structures with internal relaxation and scissor shift (Figure S4, Supporting Information) are provided in Supporting Information.

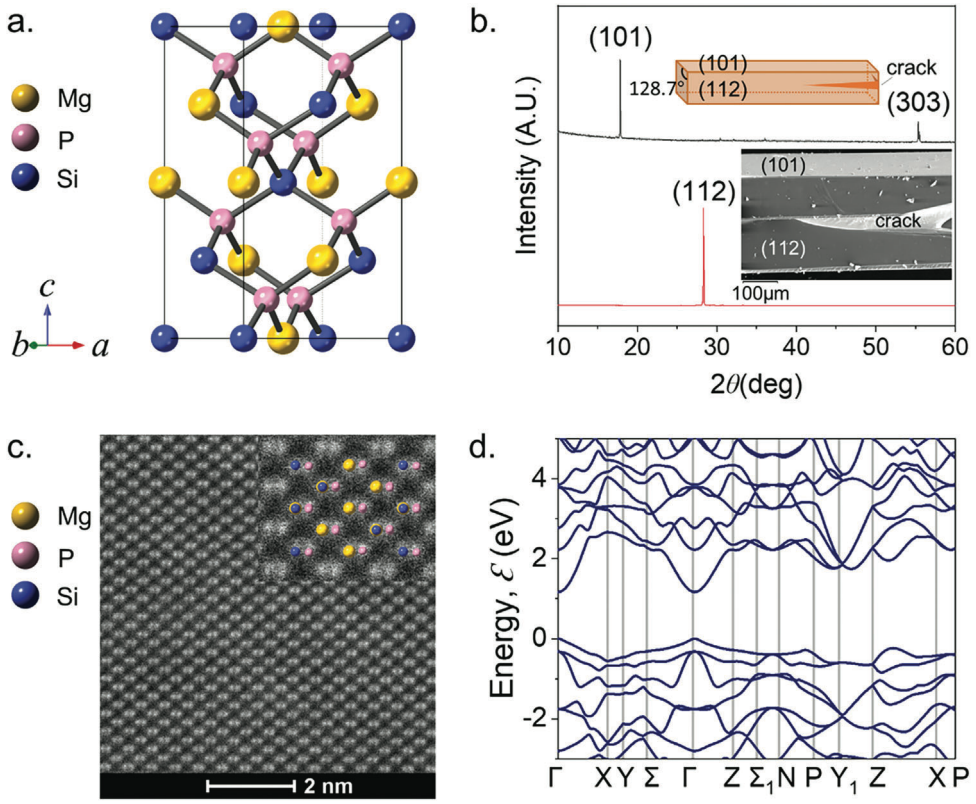

Figure 1. a) Crystal structure of $MgSiP_2$ viewed from the [120] axis. b) XRD pattern collected on the two facets of the $MgSiP_2$ single crystals, confirming the chalcopyrite structure, high crystallinity and plane orientation. Inset: a schematic (top) and an SEM image (bottom) of the crystal showing the (112) and (101) facets. c) STEM image taken from the [110] axis. Inset: A magnified HAADF-STEM image superimposed with a simulated crystal structure confirmed the phase and structure are consistent with the previously reported structure. d) Band structure of $MgSiP_2$ with internal relaxation and without scissor shift. All bands are shifted to set the valence band maximum (VBM) at 0 eV.

Next, the linear optical properties of $MgSiP_2$ are investigated. We determined the infrared transparency of $MgSiP_2$ using Fourier transform infrared (FTIR) spectroscopy equipped with a 15× objective to ensure that the beam was focused on an area with uniform thickness. The transmittance spectrum shown in **Figure 2**a was collected on the (112) plane of a single crystal with a thickness of ≈225 μm in the spectral range of 1–25 μm at room temperature. We found that $MgSiP_2$ is transparent up to ≈10.35 μm. Given that its bandgap is 2.34 eV (≈0.53 μm),[31] $MgSiP_2$ has a large transparency window of 0.53–10.35 μm. Though $AgGaS_2$, $AgGaSe_2$ and $ZnGeP_2$ are transparent further into the infrared region (13.2, 13.22, and 10.7 μm, respectively),[14,32,33] it is better than $CdSiP_2$ (9.5 μm),[25] allowing broadband tunability.

The anisotropic complex refractive indices ($\tilde{n} = n + ik$) were determined using spectroscopic ellipsometry. Since $MgSiP_2$ belongs to the tetragonal crystal system, it is a uniaxial crystal with two distinct complex refractive indices: ordinary $\tilde{n}_o$ in the plane perpendicular to the fourfold rotation axis, and extraordinary $\tilde{n}_e$ along the fourfold rotation axis.

The ellipsometry spectra were measured in two different orientations, where [11$\bar{1}$] was parallel and perpendicular to the plane of incidence. The constants $\tilde{n}_o$ and $\tilde{n}_e$ can then be extracted by simultaneously fitting the two sets of ellipsometry data with the Gaussian oscillators (Figure S5, Supporting Information), whose

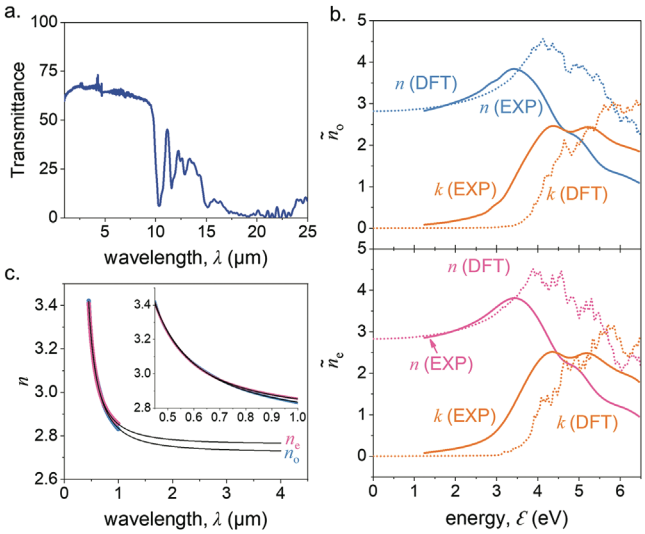

Figure 2. a) Transmittance spectrum of a single crystal $MgSiP_2$ with a thickness of ≈225 μm. b) The experimental complex ordinary (top) and extraordinary (bottom) refractive indices of $MgSiP_2$ compared with results from DFT calculations with internal relaxation and scissor shift. c) Ordinary and extraordinary refractive indices of $MgSiP_2$ and the theoretical Sellmeier fit. The inset enlarges the data in 0.45–1.0 μm to show the good fit.

Table 1. The parameters of Sellmeier equations for ordinary and extraordinary refractive indices.

n	A	B	C [μm^2]
n_o	7.423	0.3	0.06685
n_e	7.622	0.4774	0.08485

fit parameters are listed in Table S1, Supporting Information. The complex refractive indices were also computed from first principles within DFT-LDA, which show excellent qualitative and quantitative agreement with the experiments, as shown in Figure 2b. From the extrapolation of the experimental result using the Urbach absorption equation $k = k_0\, e^{(E-E_0)/E_u}$ (detailed parameters are shown in Table S2, Supporting Information),[34] the extinction coefficient k in our crystals is currently 0.05 at 1550 nm and ~0.03 at wavelengths above 3 μm; however, the first principles calculations show that k is 0.02 at 1550 nm and 7×10^{-4} above 3 μm. This indicates that the absorption can be improved if the crystals have higher purity and lower defects with better synthesis.

Since $MgSiP_2$ has a large transparency window of 0.53–10.35 μm (Figure 2a), the dispersion is small in 1–4 μm. Therefore the refractive indices n from 0.45 to 1 μm were fitted to the Sellmeier equation $n^2 = A + \frac{B}{\lambda^2 - C}$ and extrapolated to 4 μm for the SHG analysis and phase-matching calculations (Figure 2c). The parameters of the Sellmeier equations are shown in **Table 1**. The birefringence is also calculated and shown in Figure S6, Supporting Information.

Next we present the second-order NLO susceptibility of $MgSiP_2$. In the SHG process, two identical photons of frequency ω are converted into one photon of frequency 2ω when they travel through a noncentrosymmetric medium. The relationship between the induced nonlinear polarization $P_{2\omega}$ and the incident electric field E_ω can be expressed as $P_{i,\,2\omega} \propto d_{ijk}\, E_{j,\,\omega}\, E_{k,\,\omega}$, in which d is the second-order optical susceptibility tensor and the subscripts i, j, k are dummy variables describing the polarization of the various photons. To study the non-resonant SHG properties, we chose the fundamental wavelength to be 1550 nm; therefore, the resulting second-harmonic wave was 775 nm. This ensures that the SHG process occurs only within virtual states and the crystal is transparent to both wavelengths, a key requirement for an NLO crystal. Optical SHG polarimetry was employed in normal reflection geometry, as shown in **Figure 3**a.

The fundamental electric field $\boldsymbol{E}_\omega$ was linearly polarized and rotated by an angle of ψ with respect to lab axis X. A wedged crystal with a crystal plane (112) was oriented such that the $[11\bar{1}]$ and $[1\bar{1}0]$ crystal axes coincide with the lab axes X and Y, respectively. The advantage of using a wedge sample is that only the SHG generated from the front surface needs to be considered, which has proven robustness in extracting the SHG tensor.[3,36] The reflected SHG field was decomposed into p-polarized (∥) and s-polarized (⊥) by an analyzer and detected by a photo-multiplier tube. For the point group $\bar{4}2m$, the d tensor in Voigt notation is:

$$d = \begin{pmatrix} 0 & 0 & 0 & d_{14} & 0 & 0 \\ 0 & 0 & 0 & 0 & d_{14} & 0 \\ 0 & 0 & 0 & 0 & 0 & d_{36} \end{pmatrix} \quad (1)$$

The theoretical expressions for the SHG intensity in normal reflection geometry were generated by the modeling tool ♯SHAARP:[36]

$$\begin{aligned} I_X^{2\omega} &= 1.501 \times 10^{-5}(1. + \cos 2\psi)^2 d_{14}^2 \\ &\quad + \left[-2.324 \times 10^{-5} + 3.123 \times 10^{-5} \cos 2\psi \right. \\ &\quad \left. + 5.447 \times 10^{-5}(\cos 2\psi)^2 \right] d_{14} d_{36} \\ &\quad + \left[9.001 \times 10^{-6} - 4.219 \times 10^{-5} \cos 2\psi \right. \\ &\quad \left. + 4.943 \times 10^{-5}(\cos 2\psi)^2 \right] d_{36}^2 \\ I_Y^{2\omega} &= 9.532 \times 10^{-5}(\sin 2\psi)^2 d_{14}^2 \end{aligned} \quad (2)$$

The numbers are the numerical values of the relevant Fresnel coefficients (for conversion from 1550 to 775 nm) and that of the rotation matrix that transforms the crystal physics coordinates (Z_1, Z_2, Z_3) to the experimental coordinate system (X, Y, Z). The completely analytical expressions of the SHG electric field can be generated using the ♯SHAARP package;[36] it is not shown here for brevity. To obtain the d_{ij} coefficients of $MgSiP_2$, the polar plots were fitted to Equation (2) (Figure 3b) and compared with that measured on a wedged x-cut $LiNbO_3$ reference under the same experimental conditions (Figure S7, Supporting Information). The detailed analysis is explained in Supporting Information. From $I_X^{2\omega}$, we obtained the ratio of $d_{14}/d_{36} = 1.05 \pm 0.05$, and thus the two non-zero SHG coefficients are practically equal, confirming the Kleinman symmetry and the non-resonant SHG process.[37] The SHG coefficients were extracted to be $d_{14} = d_{36} = 89 \pm 5$ pm V^{-1}, surpassing the commercial NLO crystals $AgGaS_2$, $AgGaSe_2$ and $ZnGeP_2$.[24,38] To ensure that the detected signal was from the second-order NLO effect, we measured the SHG intensities as a function of incident power, as shown in Figure 3c. The SHG response demonstrates a clear quadratic dependence on the input power. When it is plotted in the logarithmic scale, the slope is 2.08 ± 0.08, confirming that the signal measured was generated by the second-order NLO effect.

Figure 3d compares the highest non-resonant SHG coefficient $MgSiP_2$ and some well-known NLO crystals. It also illustrates the general trend that the NLO susceptibility anticorrelates with the electronic bandgap of a material. Compared with $AgGaSe_2$ and $ZnGeP_2$, $MgSiP_2$ possesses both a large SHG coefficient and a larger bandgap, whereas compared to $CdSiP_2$ (84 pm V^{-1} at 4.56 μm fundamental wavelength and 93 pm V^{-1} at 1550 nm fundamental wavelength by Miller's rule), it has a slightly smaller bandgap (5%) and comparable SHG coefficient considering the error bar.

To further understand the high NLO susceptibility, first-principles calculations within DFT-LDA were carried out. The static SHG tensor d_{ij} was computed within density-functional perturbation theory (DFPT). As expected from the small structural difference, both the fully and the internally relaxed structures yield similar results with $d_{36}^{\infty} = 27$ pm V^{-1} and $d_{36}^{\infty} = 29$ pm V^{-1}, respectively. However, a difference in the cell parameters of less than 1% results in a change of the SHG coefficient of 6%. This demonstrates the high sensitivity of SHG to structural variations.[5] Without any scissor shift, d_{36}^{∞} increases

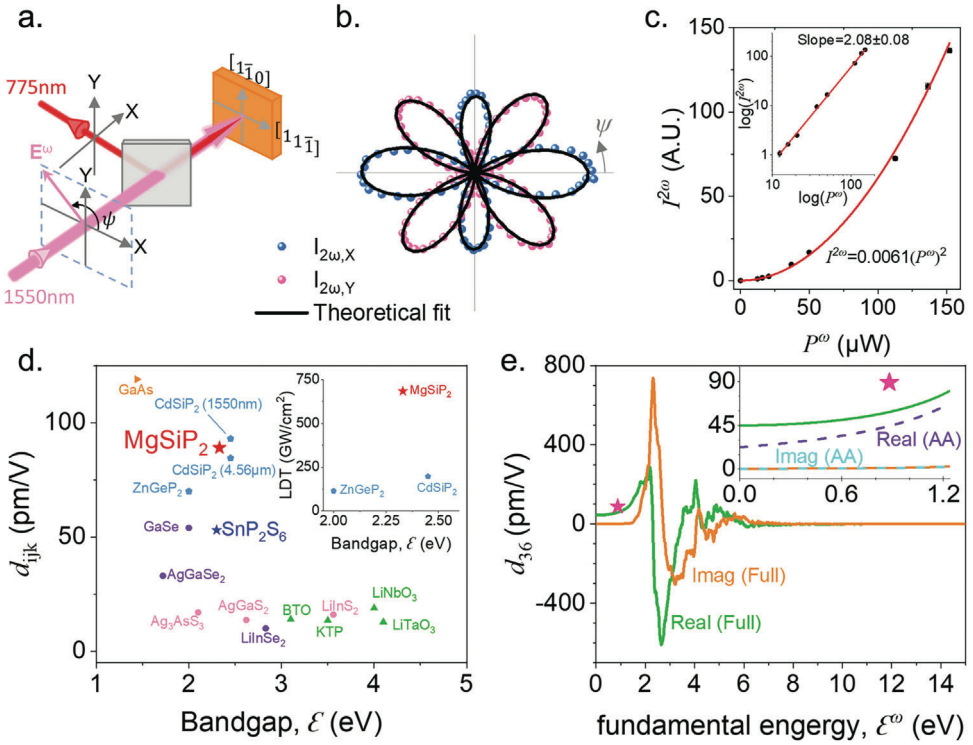

Figure 3. a) Experimental geometry of the SHG polarimetry. b) Polar plots of p-polarized (blue) and s-polarized (pink) SHG intensities of $MgSiP_2$ and the theoretical fit (black lines). c) SHG intensities of $MgSiP_2$ crystal versus incident power. The good quadratic fit confirmed the measured signal was from the SHG process. Inset: SHG intensities versus incident power in logarithmic scale. d) Comparison of SHG coefficients and bandgaps among $MgSiP_2$ (red star) and various NLO materials. The highest *non-resonant* d_{ijk} coefficients of the NLO materials are shown.[16,35] The LDTs of $MgSiP_2$, $CdSiP_2$ and $ZnGeP_2$ are illustrated in the inset. e) Energy-dependent complex d_{36} coefficient calculated by DFT with internal relaxation and scissor shift (labeled as "full"). The experimental value is shown as a pink star. In the inset, the curve obtained in the anti-resonant approximation (i.e., neglecting the anti-resonant contribution) is also displayed as a dashed line labeled AA.

to 54.859 and 57.519 pm V^{-1} for both structures, respectively. This shows the importance of the bandgap (and more generally of linear optics) in nonlinear optical calculations as summarized by Miller's rule.[39] Following a sum-over-states approach,[40] the dispersion of the SHG tensor was also calculated. As illustrated in the inset of Figure 3e, from 0 to 1.24 eV, the inclusion of anti-resonant terms is shown to affect exclusively the low-energy range of the real component by doubling its static value. This slightly increases the discrepancy with its DFPT counterpart, but the agreement with the experimental result at 1550 nm (0.8 eV) is improved despite a clear underestimation of the SHG component.

In order to physically understand the origin of the large SHG coefficient, the total response was decomposed into three different terms originating from 1) the interband transitions; 2) the intraband transitions; and 3) the modulation of the interband terms by intraband terms, as proposed in Refs.[40 and 41]. In the following, they will respectively be called "inter," "intra," and "mod." Their definition directly originates from the Genkin–Mednis approach in the mathematical treatment applied to the Hamiltonian when developing the sum-over-states equation.[42] To the best of our knowledge, there is no straightforward way to relate the "inter," "intra," and "mod" terms to distinct features of the electronic band structure. However, by simplifying the different sums, it is possible to identify the bands that contribute the most to each of these terms, as will be shown below. From Figure S8, Supporting Information, it can be seen that, in $MgSiP_2$, the total real response (resonant terms only) in the low energy range primarily originates from the "intra" term and more precisely from its 2ω resonance (see equation B2 of Ref. 40).[43] According to the following sum rule,[44]

$$R\left(\chi^{(2)}(0,0,0)\right) = \frac{2}{\pi} P \int \frac{I\left(\chi^{(2)}(-2\omega,\omega,\omega)\right)}{\omega} d\omega \quad (3)$$

the spectrum of the imaginary part of the SHG tensor is responsible for its real value in the static limit. In the present case, it appears that the high positive peak of $I(\chi^{(2)}(-2\omega,\omega,\omega)) \approx 2.27$ eV constitutes the main feature of interest (see Figure S8, Supporting Information). Its major component is also the "intra" 2ω resonant term, as expected from the above equation.

When shifting the 2ω term in accordance with its resonance, as shown in **Figure 4**a, the imaginary "intra" curves can be seen as modulations of the absorption one. This is perfectly in line with what Sipe and Ghahramani proposed originally.[40] It once again proves the importance of linear optics for the emergence of nonlinear optical phenomena, as emphasized by Miller's rule.[39] One can indeed assume that a large or abrupt absorption could favor this "intra" contribution, leading in turn to an important real value at low frequencies. This assumption and the required

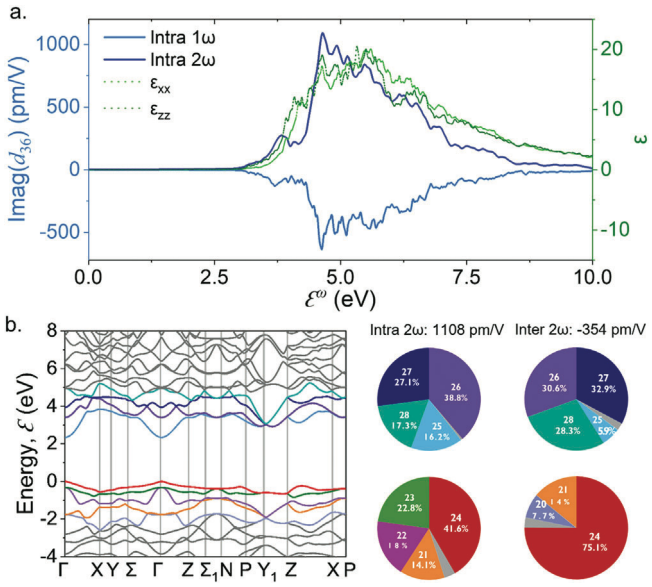

Figure 4. a) Energy dependence of the imaginary SHG "intra" 1 and 2 terms and of the xx (ordinary) and zz (extraordinary) components of the linear optical response. The 2ω curve was shifted in accordance with its resonance. b) Contributions of the different bands to the main peak of the imaginary SHG response for the main terms. Only the 3-bands interactions were considered. The bands are shifted to set the valence band maximum (VBM) at 0 eV.

interpretation of the "intra" term should be explored in further investigations.

In all the above, the "inter," "intra," and "mod" terms are a sum over two- or three-band contributions. Similar to the band-resolved analysis introduced by Lee et al.,[45] the valence and conduction bands with the largest SHG contribution were identified by summing over the bands in two different ways. The results of this analysis in the case of the main peak of $I(\chi^{(2)}(-2\omega, \omega, \omega))$ are illustrated in Figure 4b. Only the "intra" 2ω and "inter" 2ω are represented since they largely dominate the other terms (see Figure S8, Supporting Information) in this frequency range. As shown by the pie charts in the figure, the SHG mainly comes from the interaction between five bands at the top of the valence band and four bands at the bottom of the conduction band. From the projected density of states (PDOS) of Figure S9, Supporting Information, the top of the valence band corresponds to P-p orbitals, while the bottom of the conduction band can be attributed to Si-s and P-p orbitals. This emphasizes the importance of the [SiP_4] tetrahedral units as well as their geometrical arrangement.

In real applications, phase-matching is one of the most crucial criteria for efficient high-power nonlinear conversion. When the crystal achieves the phase-matching conditions, the fundamental wave and the SHG wave travel at the same speed; in other words, $n^{\omega} = n^{2\omega}$. This can only be realized in anisotropic crystals with a large enough birefringence. Since $MgSiP_2$ is a positive uniaxial crystal ($n_o < n_e$), the Type-I phase-matching condition is $n_{o,2\omega} = n_{e,\omega}(\theta_m)$ and the Type-II phase-matching condition is $n_o^{\omega} + n_e^{\omega}(\theta_m) = 2n_o^{2\omega}(\theta_m)$, where θ_m is the angle between the optical axis and the wave vector.[46] Using the above-mentioned Sellmeier equations for the refractive indices, the phase-matching conditions of $MgSiP_2$ can thus be calculated, as shown in **Figure 5**a,b. The effective d coefficient for Type I and Type II can be expressed as $d_{eff,\,I} = d_{36}\sin(2\theta_m)\cos(2\varphi)$ and $d_{eff,\,II} = -d_{36}\sin(\theta_m)\sin(2\varphi)$, where φ is the azimuthal angle as defined in Figure 5c. In practical applications, the crystal will be cut into a wafer such that the angle between the surface normal and the optical axis equals the phase-matching angle. Using Miller's rule,[39] one can estimate the value of d_{36} at other wavelengths. For example, $d_{36} \approx 81.6$ pm V^{-1} at 3.5 μm and therefore $|d_{eff,I}| = 80.2$ pm V^{-1} at $\varphi = 0°$ and $|d_{eff,II}| = 73.4$ pm V^{-1} at $\varphi = 45°$ as shown in Figure 5d.

We also assessed the LDT value of $MgSiP_2$, as it is a critical requirement for high-power laser applications. The evaluation was performed on the as-grown (112) plane of the crystal without polishing and without any antireflection coating the surfaces. A femtosecond laser system (1550 nm, 1 kHz, 100 fs) was used to generate high peak power laser pulses (up to 50 GW). During the measurement, the beam size (diameter of ~70 μm) was kept the same while the incident power was gradually increased. The surface of the crystal was inspected with an optical microscope for each trial until apparent damages appeared. $MgSiP_2$ has a giant LDT value of 684 GW cm^{-2}. For comparison, we also measured the LDTs of $ZnGeP_2$ and $CdSiP_2$ (provided by BAE Systems) using the same laser system, which are 115 and 198 GW cm^{-2}, respectively. The obtained LDT of $ZnGeP_2$ is in excellent agreement with the previously reported value.[15] We found the LDT of $MgSiP_2$ is approximately six times greater than $ZnGeP_2$ and over three times greater than $CdSiP_2$, as illustrated in the inset of Figure 3d. The detailed parameters are shown in Table S3, Supporting Information. Though its thermal conductivity is lower than that of CdSiP2 (Supporting Information), its LDT is significantly larger. The combination of large phase-matchable SHG coefficients and LDT makes $MgSiP_2$ an excellent material for high-power laser applications.

3. Conclusions

$MgSiP_2$ has been successfully synthesized and demonstrated as a high-performing infrared NLO material. The linear and nonlinear optical properties were systematically studied, indicating a large SHG coefficient of $|d_{36}| = 89 \pm 5$ pm V^{-1}, surpassing all the current commercial crystals. Importantly, it possesses a giant LDT value more than six times greater than the benchmark crystal $ZnGeP_2$. It also has a broad transparency window of 0.53–10.35 μm and can be both Type I and Type II phase-matched. These exceptional properties make it an outstanding crystal for infrared laser applications. The excellent SHG performance is shown to arise from intraband transitions involving [SiP_4] tetrahedral units, providing guidance for future NLO crystal design. Future studies should focus on exploring synthesis methods for growing larger single crystals, such as the Bridgman technique in order to make progress toward commercialization. Further, other materials systems which contain group II cations in tetrahedral coordination with similar structures appear to be promising avenues for future explorations.

4. Experimental Section

Single Crystal Synthesis—Sb Flux: $MgSiP_2$ single crystals were grown through the Sb-flux growth method. High-purity Mg turnings, Si powder,

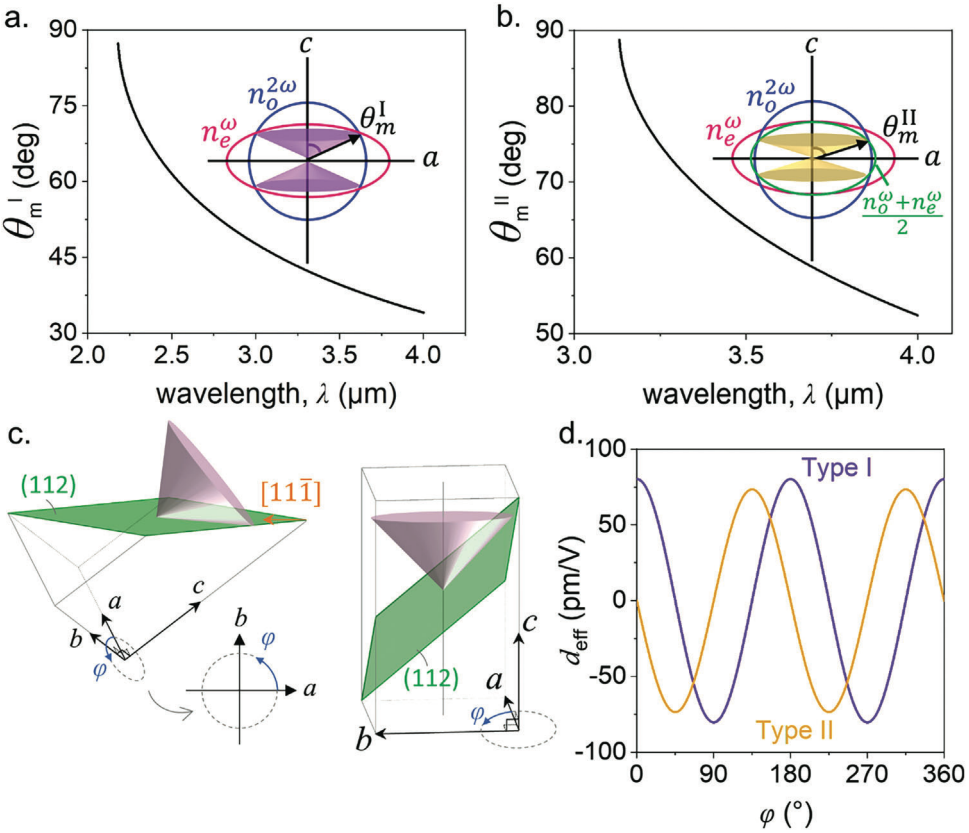

Figure 5. a) Type I and b) Type II phase-matching angles of $MgSiP_2$ at various fundamental wavelengths. c) Definition of the phase matching angle θ_m and azimuthal angle φ. d) d_{eff} for Type I and Type II phase-matching conditions of $MgSiP_2$ versus the azimuthal angle φ.

and P powder with a molar ratio of 1:1:2 were put into alumina crucibles. Sb powder was added to the alumina crucible and formed a 16.6 mass percent solution with the raw materials. The alumina crucibles were then put into clear silica tubes and sealed under vacuum with the typical vacuum level ranging from 3×10^{-4} torr to 9×10^{-4} torr. The sealed ampoules were then placed inside a muffle furnace and heated to 1100 °C for 48 h to ensure homogeneous melt, followed by slow cooling at 3 °C h^{-1} to 650 °C. The $MgSiP_2$ crystals were separated from the Sb flux through centrifugation. The sealed tube was removed from the furnace at 650 °C, above the Sb melting point, and then immediately centrifugated it to remove the Sb flux from the small crucible. After centrifugation, the crystals remained in the crucible while the Sb flux in liquid form spun off. The needle-like $MgSiP_2$ single crystals were well separated from the flux.

The typical mass of individual pieces of crystals ranges from 1 to 5 mg. The total mass of crystals from a batch depends on not only the amount of source materials used for growth but also the cooling rate during the growth and many other factors. The total crystal mass of a batch typically ranges from ~10mg to ~100mg.

R. T. Trykozko previously reported growth of $MgSiP_2$ using Sb flux.[27] Compared to their growth method, this work increased the heating time at a higher temperature to ensure a homogeneous melt of raw materials. The cooling rate was decreased to 3 °C h^{-1} to improve crystal size and quality. Centrifugation was used to remove Sb flux, which helped to get a cleaner crystal surface than the chemical method of removing flux reported in Ref. 27.[27]

Single Crystal Synthesis—Sn Flux: The Sn flux method was modified based on the growth method by A. J. Springthorpe and J. G. Harrison.[26] Stoichiometric quantities of high-purity Mg turnings, Si powder, and P powder were put into alumina crucibles. Sn powder was added to the alumina crucible and formed a 10 molar percent solution with the raw materials. The alumina crucible was then put in a quartz tube and sealed under vacuum. The ampoule was then heated to 1100 °C for 24 h, followed by slow cooling to 400 °C in 240 h. Centrifugation was used to remove Sn flux when the temperature reached 400 °C.

Spectroscopic Ellipsometry: Spectroscopic ellipsometry was carried out using Woollam M-2000F spectroscopic ellipsometers with a focused beam. The measurement was performed on the (101) plane of $MgSiP_2$ in the spectral range of 0.2–1.0 μm. The (101) plane of $MgSiP_2$ was used because the angle between the optic axis (parallel to the [001] direction) and the (101) plane is ~29.5°; therefore, the ellipsometry data will have more contribution from $\tilde{n}_e$ as compared to the (112) plane (~38.7°). Two sets of data were collected when the [11$\bar{1}$] was parallel and perpendicular to the plane of incidence. The anisotropic complex refractive indices were extracted by fitting the ellipsometric spectra to Gaussian oscillators. Each Gaussian oscillator includes an amplitude A, a broadening parameter B, and the central energy E_0, as shown in Table S1, Supporting Information.

SHG Measurement: The SHG measurement was performed in normal reflection geometry, shown in Figure 3a. The 1550 nm fundamental laser beam was generated by Spirit-NOPA-VISIR Laser from Spectra-Physics (100 fs, 1 MHz). During the measurement, the linearly polarized incident beam was rotated by an angle of φ using a half waveplate from the lab X axis. The SHG intensities were divided into p-polarized and s-polarized and then recorded by a photo-multiplier tube. A wedged x-cut $LiNbO_3$ (MTI Corporation) was used as a reference.

First-Principles Calculations: In this work, all the simulations were performed with the ABINIT software[47–49] in the framework of density-functional theory (DFT) for the ground-state (GS) calculations and the density-functional perturbation theory (DFPT) for the response functions.[50] The input generation, the workflows, and the analyses of the results were automated with the AbiPy python package. The wavefunctions were expanded on a plane-wave basis set using a kinetic energy cutoff of 42 Ha, in combination with scalar relativistic Optimized

Norm-Conserving Vanderbilt Pseudopotentials (ONCVPSP) from the PseudoDojo.[51,52] The DFT and DFPT calculations adopted the local-density approximation (LDA) for the exchange-correlation energy.[53] As an alternative, the Perdew-Burke-Ernzerhof generalized-gradient approximation was also tested for the ground-state calculations, but it did not lead to any significant changes.[54]

All relaxations were performed using a 10 × 10 × 10 Monkhorst-Pack k-point mesh to sample the Brillouin zone.[55,56] The structure was optimized until the maximum force on each atom was lower than 2.5 meV Å^{-1}. The relaxation of the tetragonal cell parameters (a and c) resulted in an excellent agreement with their experimental values:

$$\frac{\left|a_{exp} - a_{LDA}\right|}{a_{exp}} = 0.75\% \quad \frac{\left|c_{exp} - c_{LDA}\right|}{c_{exp}} = 0.58\% \tag{4}$$

Since reliable third-order energy derivatives typically require a denser sampling of the Brillouin zone, a 16 × 16 × 16 Monkhorst-Pack k-point mesh was adopted for all the calculations other than the relaxations. For the optical properties, a scissor shift was systematically applied on all conduction bands to match the experimental bandgap of 2.34 eV.

The static high-frequency (clamped-ions) dielectric and SHG tensors were first computed within DFPT using ABINIT. Thanks to the Optic utility of ABINIT, their frequency-dependent counterparts were calculated in the independent-particle approximation with a sum-over-states approach as developed by Hughes and Sipe.[43] The inclusion of the anti-resonant terms results from an unpublished modification of the Optic utility. A total of 60 empty conduction bands (i.e., all the bands up to 25 eV above the valence band maximum) were included in the computation. Divergences were avoided by smoothing the spectrum with a broadening of 0.002 Ha (54 meV). The dielectric function provides the refractive index and extinction coefficients following the usual relations.

Supporting Information

Supporting Information is available from the Wiley Online Library or from the author.

Acknowledgements

J.H. and V.G. acknowledge primary support from NSF DMR-2210933 for work since September 2022. J.H. and V.G. also acknowledge partial support from the Air Force Office of Scientific Research Grant number FA9550-19-1-0243 for work prior to September 2022. Support for crystal growth and characterization was provided by the National Science Foundation through the Penn State 2D Crystal Consortium-Materials Innovation Platform (2DCC-MIP) under NSF cooperative agreements DMR-2039351. Partial crystal growth efforts made by a graduate student (Y.G.) are also supported by the U.S. Department of Energy under grants DE-SC0019068. Computational resources have been provided by the supercomputing facilities of the Université catholique de Louvain (CISM/UCL) and the Consortium des Équipements de Calcul Intensif en Fédération Wallonie Bruxelles (CÉCI) funded by the Fond de la Recherche Scientifique de Belgique (F.R.S.-FNRS) under convention 2.5020.11 and by the Walloon Region. The authors acknowledge U.S. Department of Energy, Office of Science, Basic Energy Sciences, Award No. DE-SC0020145 for supporting the development of Shaarp. The authors thank Peter Schunemann and Kevin Zawilski for the scientific discussions and for offering the $ZnGeP_2$ and $CdSiP_2$ crystals.

Conflict of Interest

The authors declare no conflict of interest.

Data Availability Statement

The data that support the findings of this study are available from the corresponding author upon reasonable request.

Keywords

diamond-like structure, nonlinear optical crystals, second harmonic generations

Received: May 5, 2023
Revised: June 15, 2023
Published online:

[1] F. Liang, L. Kang, Z. Lin, Y. Wu, *Cryst. Growth Des.* **2017**, *17*, 2254.
[2] B. M. Oxley, J. Bin Cho, A. K. Iyer, M. J. Waters, J. He, N. C. Smith, C. Wolverton, V. Gopalan, J. M. Rondinelli, J. I. Jang, M. G. Kanatzidis, *J. Am. Chem. Soc.* **2022**, *144*, 13903.
[3] J. He, A. K. Iyer, M. J. Waters, S. Sarkar, R. Zu, J. M. Rondinelli, M. G. Kanatzidis, V. Gopalan, *Adv. Opt. Mater.* **2022**, *10*, 2101729.
[4] I. Chung, M. G. Kanatzidis, *Chem. Mater.* **2014**, *26*, 849.
[5] J. He, S. H. Lee, F. Naccarato, G. Brunin, R. Zu, Y. Wang, L. Miao, H. Wang, N. Alem, G. Hautier, G.-M. Rignanese, Z. Mao, V. Gopalan, *ACS Photonics* **2022**, *9*, 1724.
[6] A. K. Iyer, J. He, H. Xie, D. Goodling, D.-Y. Chung, V. Gopalan, M. G. Kanatzidis, *Adv. Funct. Mater.* **2022**, *33*, 2211969.
[7] C. T. Chen, B. C. Wu, A. D. Jiang, G. M. You, *Sci. Sin. B (Englisch Ed.* **1984**, *7*, 595.
[8] G. D. Boyd, R. C. Miller, K. Nassau, W. L. Bond, A. Savage, *Appl. Phys. Lett.* **1964**, *5*, 234.
[9] C. Chen, Y. Wu, A. Jiang, B. Wu, G. You, R. Li, S. Lin, *J. Opt. Soc. Am. B* **1989**, *6*, 616.
[10] M. C. Ohmer, R. Pandey, *MRS Bull.* **1998**, *23*, 16.
[11] P. G. Schunemann, K. L. Schepler, P. A. Budni, *MRS Bull.* **1998**, *23*, 45.
[12] H. J. Krause, W. Daum, *Appl. Phys. B Photophys. Laser Chem.* **1993**, *56*, 8.
[13] Y. Kim, I. Seo, S. W. Martin, J. Baek, P. Shiv Halasyamani, N. Arumugam, H. Steinfink, *Chem. Mater.* **2008**, *20*, 6048.
[14] U. Simon, Z. Benko, M. W. Sigrist, R. F. Curl, F. K. Tittel, *Appl. Opt.* **1993**, *32*, 6650.
[15] V. Petrov, F. Rotermund, F. Noack, P. Schunemann, *Opt. Lett.* **1999**, *24*, 414.
[16] D. N. Nikogosyan, *Nonlinear Optical Crystals: A Complete Survey*, Springer Science & Business Media, Berlin, Germany **2006**.
[17] K. T. Zawilski, P. G. Schunemann, T. C. Pollak, D. E. Zelmon, N. C. Fernelius, F. K. Hopkins, *J. Cryst. Growth* **2010**, *312*, 1127.
[18] R. L. Byer, H. Kildal, R. S. Feigelson, *Appl. Phys. Lett.* **1971**, *19*, 237.
[19] K. E. Woo, J. Wang, K. Wu, K. Lee, J. A. Dolyniuk, S. Pan, K. Kovnir, *Adv. Funct. Mater.* **2018**, *28*, 1801589.
[20] J. Xiao, S. Zhu, B. Zhao, B. Chen, H. Liu, Z. He, *Mater. Res. Express* **2018**, *5*, 035907.
[21] A. Petukhov, W. Lambrecht, B. Segall, *Phys. Rev. B* **1994**, *49*, 4549.
[22] B. Kocak, Y. O. Ciftci, G. Surucu, *J. Electron. Mater.* **2017**, *46*, 247.
[23] J. Chen, Q. Wu, H. Tian, X. Jiang, F. Xu, X. Zhao, Z. Lin, M. Luo, N. Ye, *Adv. Sci.* **2022**, *9*, 2105787.
[24] G. C. Catella, D. Burlage, *MRS Bull.* **1998**, *23*, 28.
[25] J. Wei, J. M. Murray, F. K. Hopkins, D. M. Krein, K. T. Zawilski, P. G. Schunemann, S. Guha, *Opt. OSA Technical Digest (Online)*. **2017**, NTu3A.8.
[26] A. J. Springthorpe, J. G. Harrison, *Nature* **1969**, *222*, 977.
[27] R. T. Trykozko, *Mater. Res. Bull.* **1975**, *10*, 489.

[28] A. E. Kokh, V. Mishchenko, V. D. Antsygin, A. M. Yurkin, N. G. Kononova, V. A. Guets, Y. K. Nizienko, A. I. Zakharchenko, *Laser Mater. Cryst. Growth Nonlinear Mater. Devices* **1999**, *3610*, 139.
[29] J. E. Jaffe, A. Zunger, *Phys. Rev. B* **1984**, *29*, 1882.
[30] V. L. Shaposhnikov, A. V. Krivosheeva, V. E. Borisenko, J.-L. Lazzari, F. A. d'Avitaya, *Phys. Rev. B* **2012**, *85*, 205201.
[31] G. Ambrazevičius, G. Babonas, Y. V. Rud, A. Šileika, *Phys. status solidi* **1981**, *106*, 85.
[32] G. C. Bhar, R. C. Smith, *Phys. Status Solidi* **1972**, *13*, 157.
[33] B. Ray, A. J. Payne, G. J. Burrell, *Phys. status solidi* **1969**, *35*, 197.
[34] F. Urbach, *Phys. Rev.* **1953**, *92*, 1324.
[35] N. Itoh, T. Fujinaga, T. Nakau, *Jpn. J. Appl. Phys.* 951, **1978**, *17*.
[36] R. Zu, B. Wang, J. He, J.-J. Wang, L. Weber, L.-Q. Chen, V. Gopalan, *npj Comput. Mater.* **2022**, *8*, 246.
[37] D. A. Kleinman, *Phys. Rev.* **1962**, *126*, 1977.
[38] G. Boyd, H. Kasper, J. McFee, F. Storz, *IEEE J. Quantum Electron.* **1972**, *8*, 900.
[39] R. C. Miller, *Appl. Phys. Lett.* **1964**, *5*, 17.
[40] J. E. Sipe, E. Ghahramani, *Phys. Rev. B* **1993**, *48*, 11705.
[41] S. Sharma, J. K. Dewhurst, C. Ambrosch-Draxl, *Phys. Rev. B* **2003**, *67*, 165332.
[42] V. N. Genkin, P. M. Mednis, *Sov. Phys. JETP* **1968**, *27*, 609.
[43] J. L. P. Hughes, J. E. Sipe, *Phys. Rev. B* **1996**, *53*, 10751.
[44] W. R. L. Lambrecht, S. N. Rashkeev, *Phys. status solidi* **2000**, *217*, 599.
[45] M.-H. Lee, C.-H. Yang, J.-H. Jan, *Phys. Rev. B* **2004**, *70*, 235110.
[46] W. Zhang, H. Yu, H. Wu, P. S. Halasyamani, *Chem. Mater.* **2017**, *29*, 2655.
[47] X. Gonze, F. Jollet, F. A. Araujo, D. Adams, B. Amadon, T. Applencourt, C. Audouze, J.-M. Beuken, J. Bieder, A. Bokhanchuk, E. Bousquet, F. Bruneval, D. Caliste, M. Côté, F. Dahm, F. Da Pieve, M. Delaveau, M. Di Gennaro, B. Dorado, C. Espejo, G. Geneste, L. Genovese, A. Gerossier, M. Giantomassi, Y. Gillet, D. R. Hamann, L. He, G. Jomard, J. L. Janssen, S. Le Roux, et al., *Comput. Phys. Commun.* **2016**, *205*, 106.
[48] X. Gonze, B. Amadon, G. Antonius, F. Arnardi, L. Baguet, J.-M. Beuken, J. Bieder, F. Bottin, J. Bouchet, E. Bousquet, N. Brouwer, F. Bruneval, G. Brunin, T. Cavignac, J.-B. Charraud, W. Chen, M. Côté, S. Cottenier, J. Denier, G. Geneste, P. Ghosez, M. Giantomassi, Y. Gillet, O. Gingras, D. R. Hamann, G. Hautier, X. He, N. Helbig, N. Holzwarth, Y. Jia, et al., *Comput. Phys. Commun.* **2020**, *248*, 107042.
[49] A. H. Romero, D. C. Allan, B. Amadon, G. Antonius, T. Applencourt, L. Baguet, J. Bieder, F. Bottin, J. Bouchet, E. Bousquet, F. Bruneval, G. Brunin, D. Caliste, M. Côté, J. Denier, C. Dreyer, P. Ghosez, M. Giantomassi, Y. Gillet, O. Gingras, D. R. Hamann, G. Hautier, F. Jollet, G. Jomard, A. Martin, H. P. C. Miranda, F. Naccarato, G. Petretto, N. A. Pike, V. Planes, et al., *J. Chem. Phys.* **2020**, *152*, 124102.
[50] X. Gonze, C. Lee, *Phys. Rev. B* **1997**, *55*, 10355.
[51] D. R. Hamann, *Phys. Rev. B* **2013**, *88*, 85117.
[52] M. J. van Setten, M. Giantomassi, E. Bousquet, M. J. Verstraete, D. R. Hamann, X. Gonze, G.-M. Rignanese, *Comput. Phys. Commun.* **2018**, *226*, 39.
[53] J. P. Perdew, Y. Wang, *Phys. Rev. B* **1992**, *45*, 13244.
[54] J. P. Perdew, K. Burke, M. Ernzerhof, *Phys. Rev. Lett.* **1996**, *77*, 3865.
[55] H. J. Monkhorst, J. D. Pack, *Phys. Rev. B* **1976**, *13*, 5188.
[56] J. D. Pack, H. J. Monkhorst, *Phys. Rev. B* **1977**, *16*, 1748.